Science Advances

AAAS

advances.sciencemag.org/cgi/content/full/3/6/e1603213/DC1

Supplementary Materials for

Compressed glassy carbon: An ultrastrong and elastic interpenetrating graphene network

Meng Hu, Julong He, Zhisheng Zhao, Timothy A. Strobel, Wentao Hu, Dongli Yu, Hao Sun, Lingyu Liu, Zihe Li, Mengdong Ma, Yoshio Kono, Jinfu Shu, Ho-kwang Mao, Yingwei Fei, Guoyin Shen, Yanbin Wang, Stephen J. Juhl, Jian Yu Huang, Zhongyuan Liu, Bo Xu, Yongjun Tian

Published 9 June 2017, *Sci. Adv.* **3**, e1603213 (2017)
DOI: 10.1126/sciadv.1603213

This PDF file includes:

- fig. S15. Comparison of thermal stability of compressed GC (*Com*.GC-3) with raw GC at air and inert argon (Ar) or nitrogen (N_2) conditions, respectively.

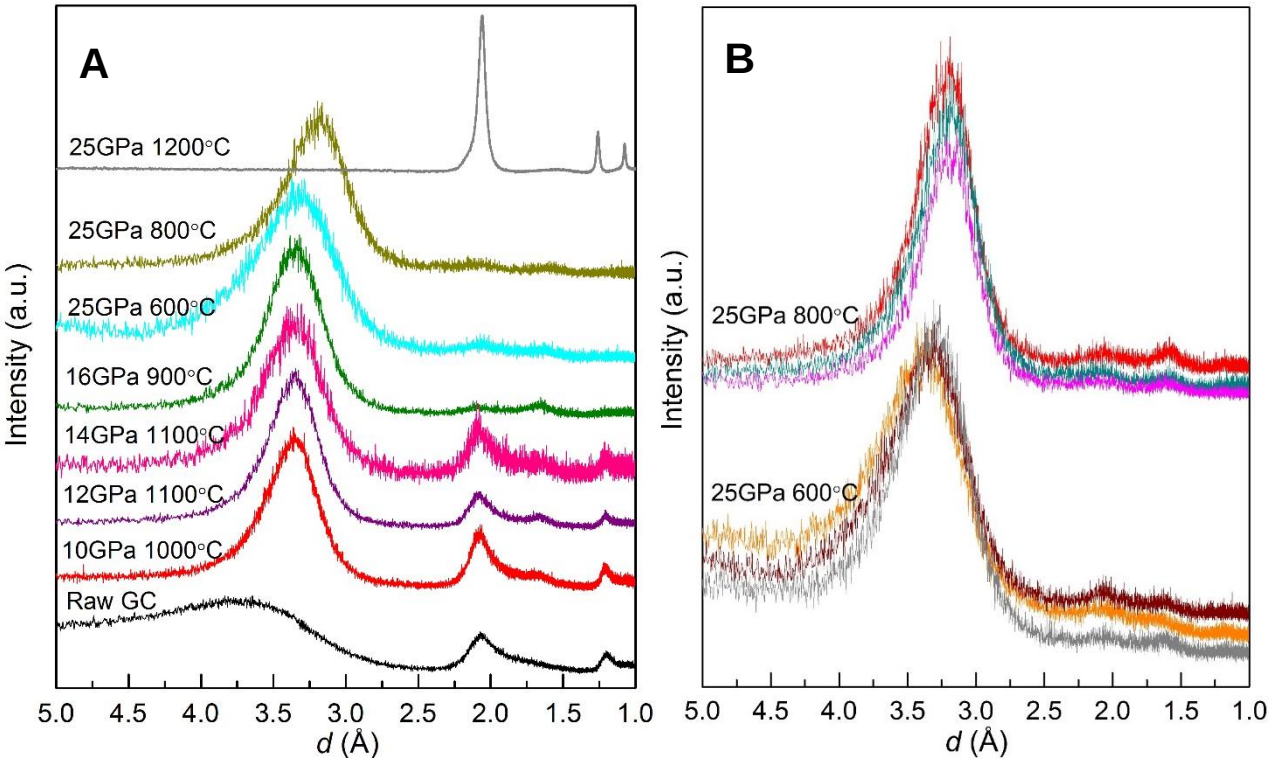

fig. S1. XRD of compressed GCs recovered after compressing raw GC at pressures of 10 to 25 GPa and temperatures of 600° to 1200°C. (**A**) The compressed GCs recovered from 10-16 GPa and 900-1100 °C have the similar interlayer distance of ～3.36 Å with that of compressed GC from 25 GPa and 600 °C (also see their similar mechanical properties shown in fig. S8 below). Notably, diamond is recovered after compressing raw GC at 25 GPa and 1200 °C, and the small broad peak near 1.6 Å, corresponding to the higher-order diffraction between graphite-like layers, indicates that there was some residual compressed GCs in the product. (**B**) X-ray diffraction of three *Com*.GC-2 and three *Com*.GC-3 samples synthesized at 25 GPa/600 °C and 25 GPa/800 °C, respectively, showing good reproducibility.

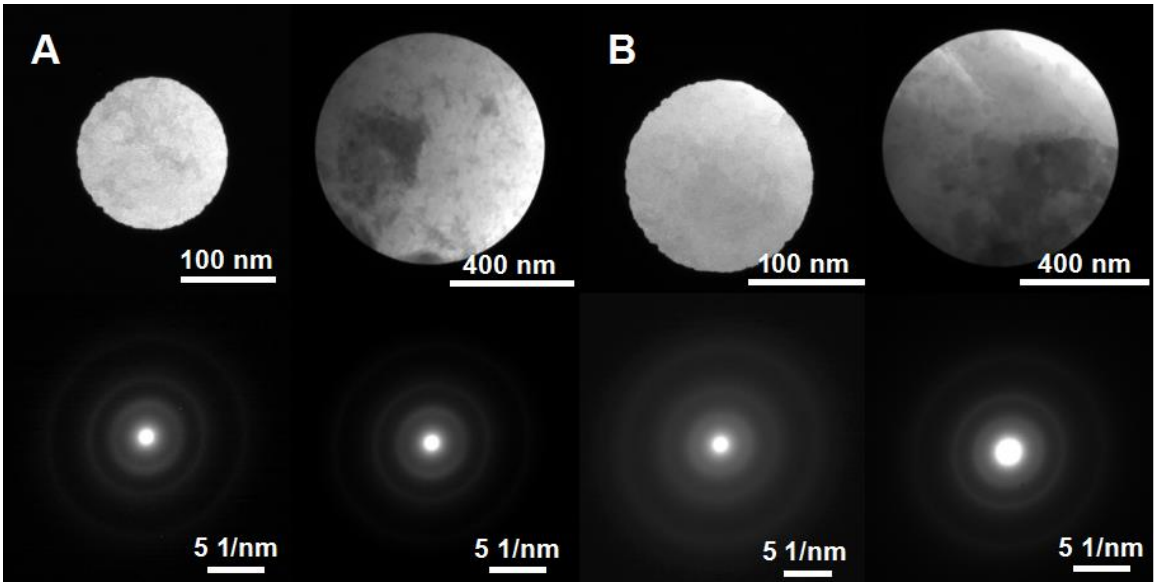

fig. S2. SAED patterns of compressed GCs measured at different length scales. (**A**, **B**) The selected diffraction area sizes and corresponding patterns from *Com*.GC-2 and *Com*.GC-3, respectively. The diffraction patterns were collected from linear dimensions of ～150 nm and 800 nm, respectively. At such large area, there is no diffraction orientation in comparison with the local order in several nanometers (Fig. 2A and fig. S3), showing the typical amorphous properties with long-range disorder and short-range order.

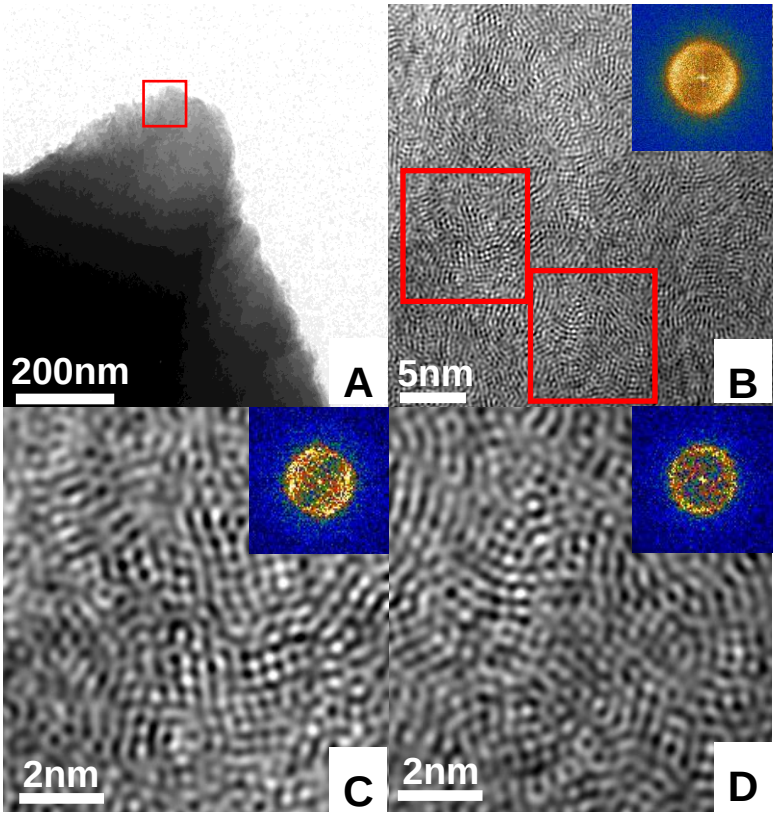

fig. S3. Local order in compressed GC. (**A**) The bright field TEM image. (**B**) HRTEM images of (A) marked region showing the interpenetrating graphene networks. (**C**, **D**) Enlarged HRTEM images corresponding to the local regions marked in (B). The domains of locally-ordered carbon nanolattices persist across lateral dimensions of 1-5 nm and exhibit lattice spacings of 3-5 Å. Insets in (B, C, D), FFT images corresponding to the respective HRTEM regions showing the primary *d*-spacing in the range of 3-5 Å from the graphite-like interlayer information. The used sample was *Com*.GC-3.

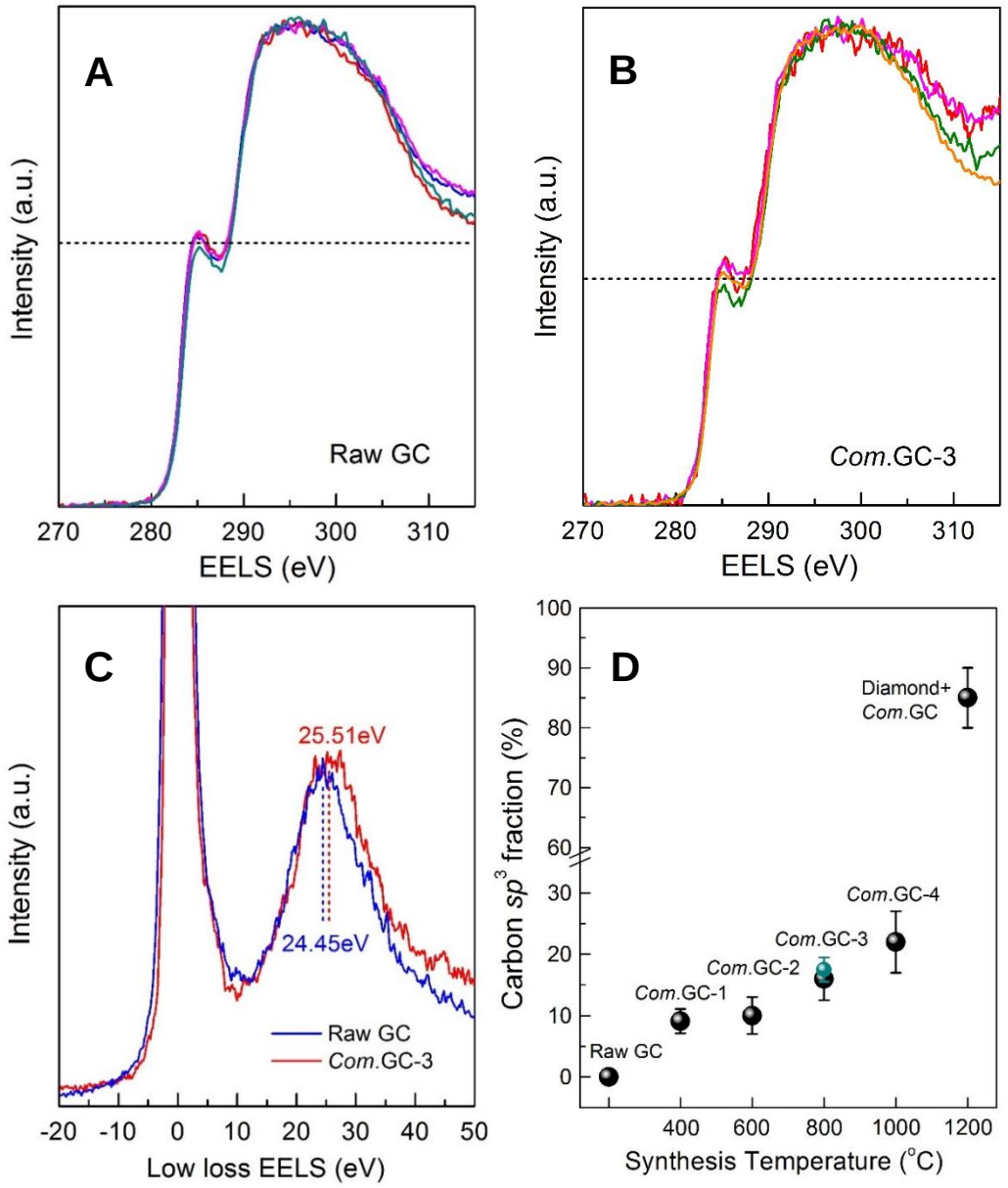

fig. S4. The sp^3 component of compressed GCs measured at ambient condition. (**A**, **B**) EELS of raw GC and *Com.*GC-3, respectively collected at four randomly selected areas. The slight intensity changes of the 1s-π* peak at 285 eV may be due to the small difference in the microstructure. The *Com.*GC-3 had a lower fraction of the sp^2 signal peak at 285 eV with respect to raw GC, indicating the formation of partial sp^3 bonding in the predominantly sp^2-based framework. (**C**) Low loss EELS of raw GC and *Com.*GC-3. The peak at 25.51 eV for *Com*.GC-3 is shifted to higher energy loss in comparison with that at 24.45 eV for raw GC, indicating an increase of sp^3 bonds. (**D**) The sp^3 fraction in compressed GCs recovered from 25 GPa and different temperatures. Error bars incorporate the effects from slight variations across multiple measurement positions. The values marked by black balls were obtained with all-sp^2 raw GC as a reference, and the fraction marked by dark-cyan ball was estimated from *Com.*GC-3 relative to all-sp^2 carbon black (fig. S5A), which fits perfectly with the data trend.

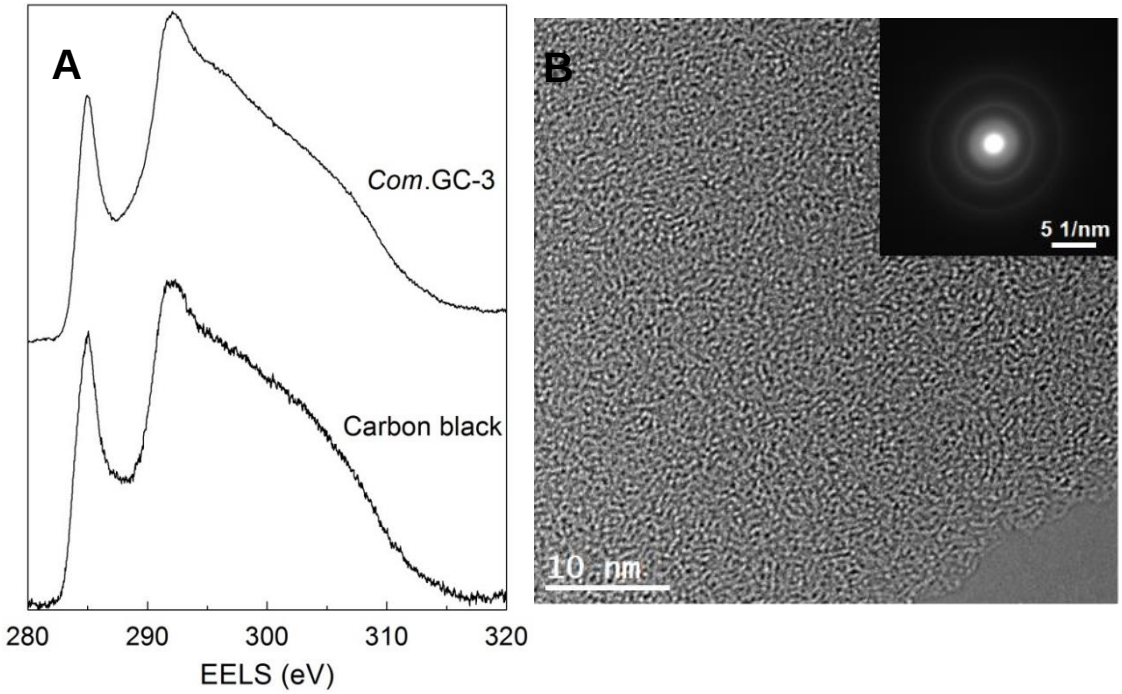

fig. S5. The sp^3 component of compressed GC and microstructure of raw GC. (**A**) EELS of *Com.*GC-3 in comparison with all-sp^2 graphitized carbon black. The *Com.*GC-3 had a slightly lower fraction of the sp^2 signal peak at 285 eV with respect to carbon black, indicating the formation of partial sp^3 bonding in the predominantly sp^2-based framework. The TEM sample of *Com.*GC-3 was prepared by focused ion beam milling, and then EELS was collected by a monochromated, aberration-corrected FEI Titan^3 60-300 S/TEM at Pennsylvania State University with an accelerating voltage of 80 kV and a high energy resolution of 170 meV. (**B**) HRTEM and SAED patterns of raw GC showing the typical disordered features. It is noted that the TEM results in this article, except that in fig. S5A, were all from the samples prepared by the common crushing/grinding method.

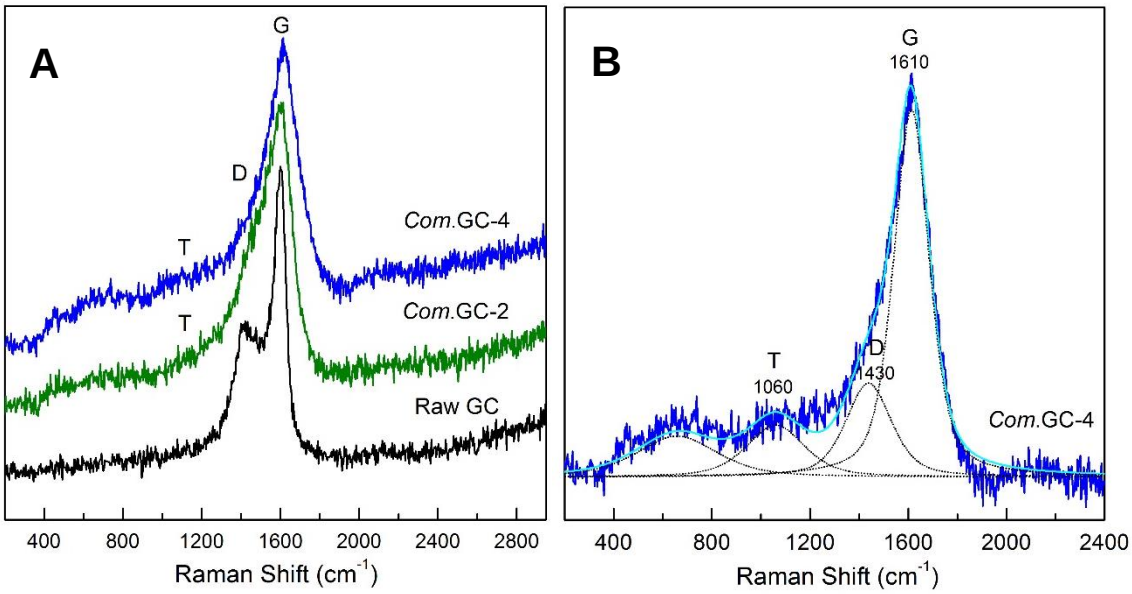

fig. S6. UV Raman spectroscopy of compressed GCs. (**A**, **B**) Original and fitted peaks, respectively. Like other amorphous carbon, the typical G band (～1600 cm^{-1}) and D band (～1400 cm^{-1}) were also found in the compressed GCs, indicating predominantly sp^2 character. The T peak lying around 1060 cm^{-1} appears in UV Raman due to the sp^3 vibrations (*19*). In addition, the decreased I(D)/I(G) intensity ratios compared with raw GC are also consistent with an increased fraction of sp^3 carbon (*20*). The Raman excitation wavelength is 325 nm.

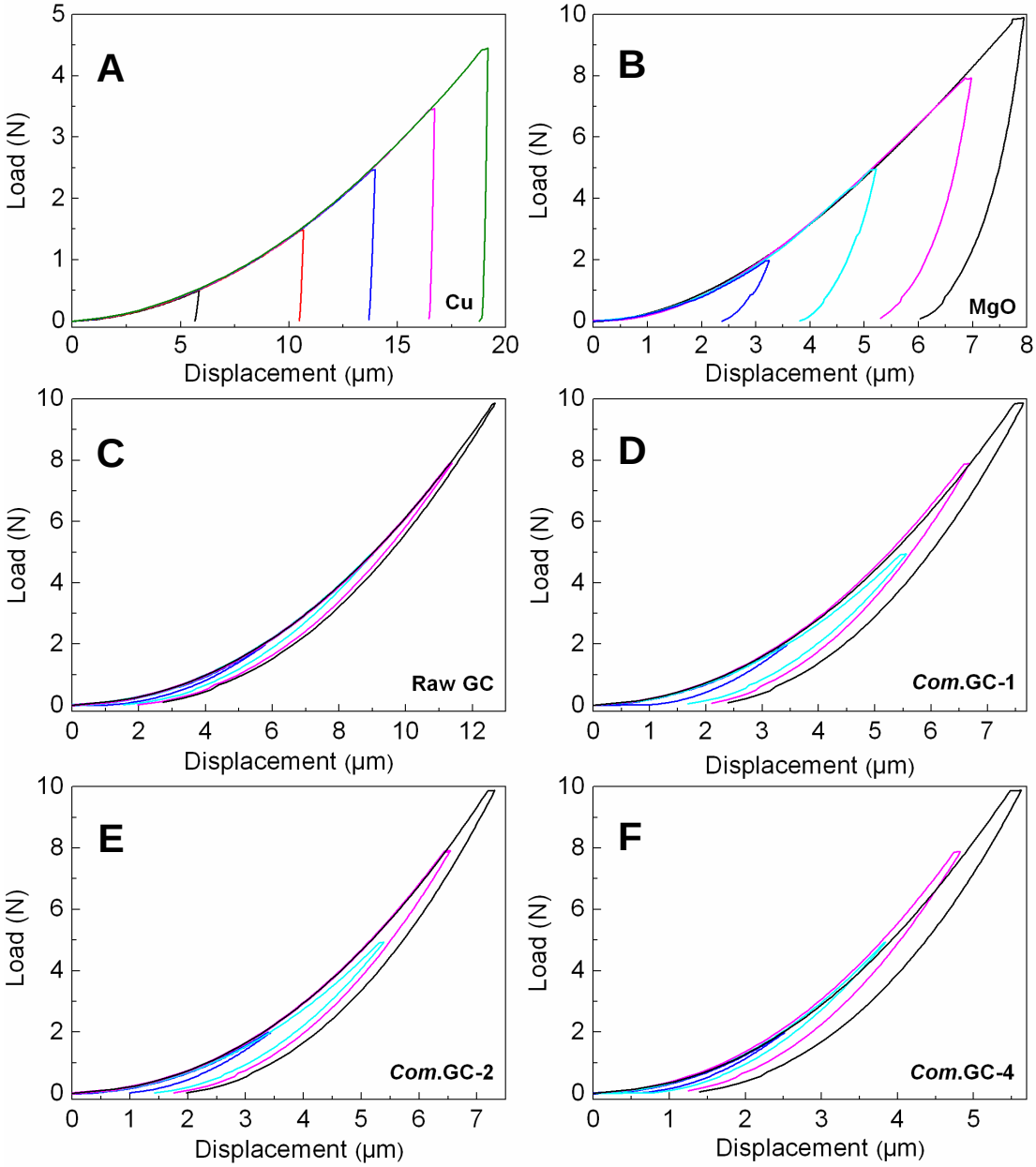

fig. S7. The loading/unloading-displacement curves of compressed GCs in comparison with raw GC, Cu, and MgO. The results are shown in (**A**) to (**F**). The *Com*.GC-1, *Com*.GC-2, *Com*.GC-3, and *Com*.GC-4 were recovered from 25 GPa and temperatures of 400°, 600°, 800°, and 1000°C, respectively. The applied loads were 0.49, 1.47, 2.45, 3.43, 4.41 N for Cu, and 1.96, 4.9, 7.84, 9.8 N for MgO and compressed GCs, respectively. The applied loading time to peak load was 15s, the peak holding time was 10s, and the unloading time was 15s. During indentation, the copper experienced complete plastic deformation, and MgO underwent partial elastic recovery after unloading. In comparison, the compressed GCs show significant elastic recovery from indentation upon unloading. Notably, the displacement depths of indenter in compressed GCs are obviously less than that of raw GC at the same load, indicating the increased hardness.

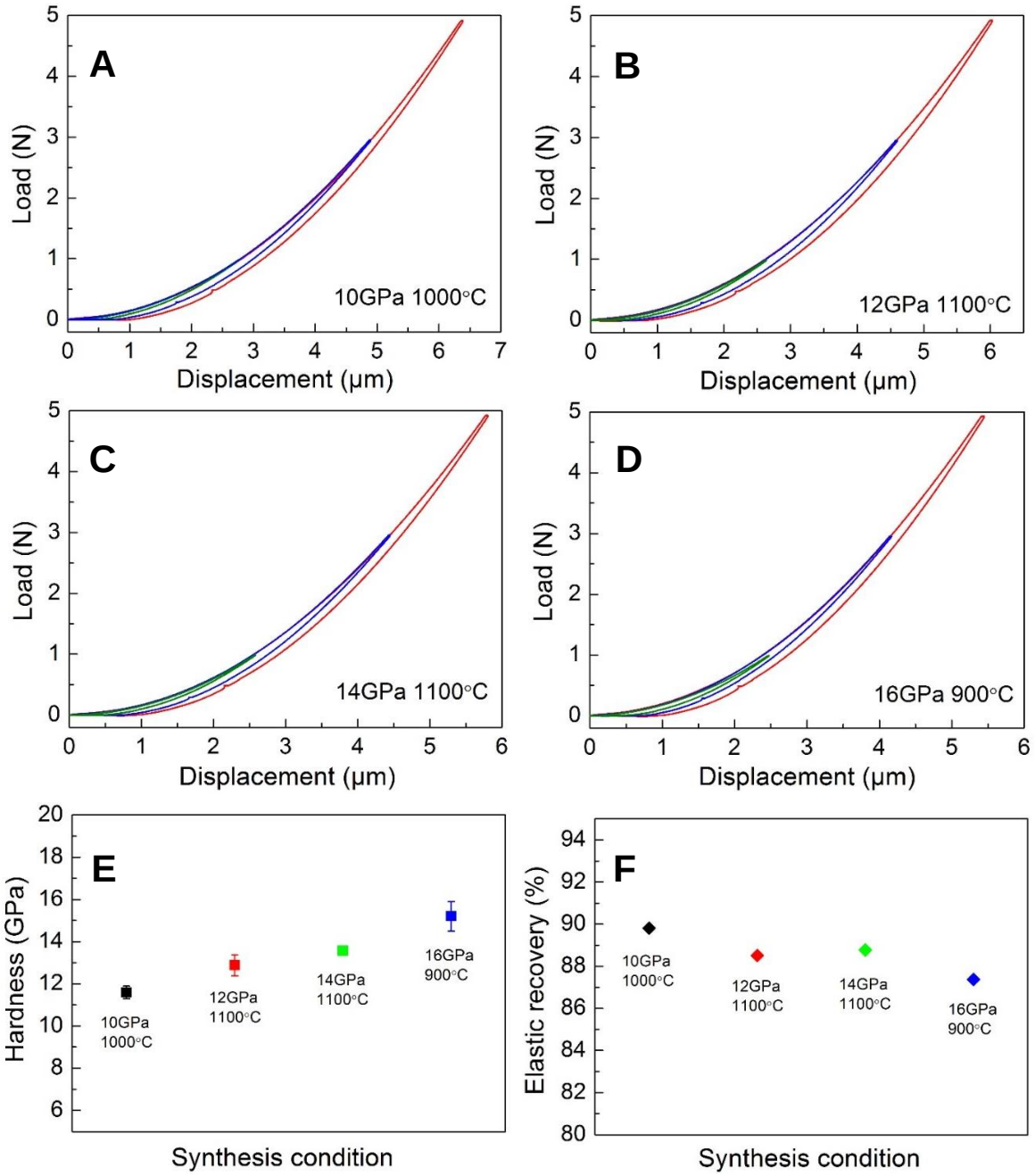

fig. S8. The loading/unloading-displacement curves, indentation hardness, and elastic recovery of compressed GCs synthesized at moderate pressures and temperatures. The results are shown in (**A**) to (**F**). The applied loads were 0.98, 2.94, and 4.9 N, respectively. The applied loading time to peak load was 15s, the peak holding time was 10s, and the unloading time was 15s. These compressed GCs not only have similar structures (see XRD in fig. S1A), but also have similar hardness and elastic recovery. Their hardness values are significantly higher than that of raw GC, and are comparable to that recovered from 25 GPa and 600 °C (*Com*.GC-2). Moreover, their elastic recoveries are even better than those recovered from high pressure of 25 GPa (Fig. 3C and fig. S7).

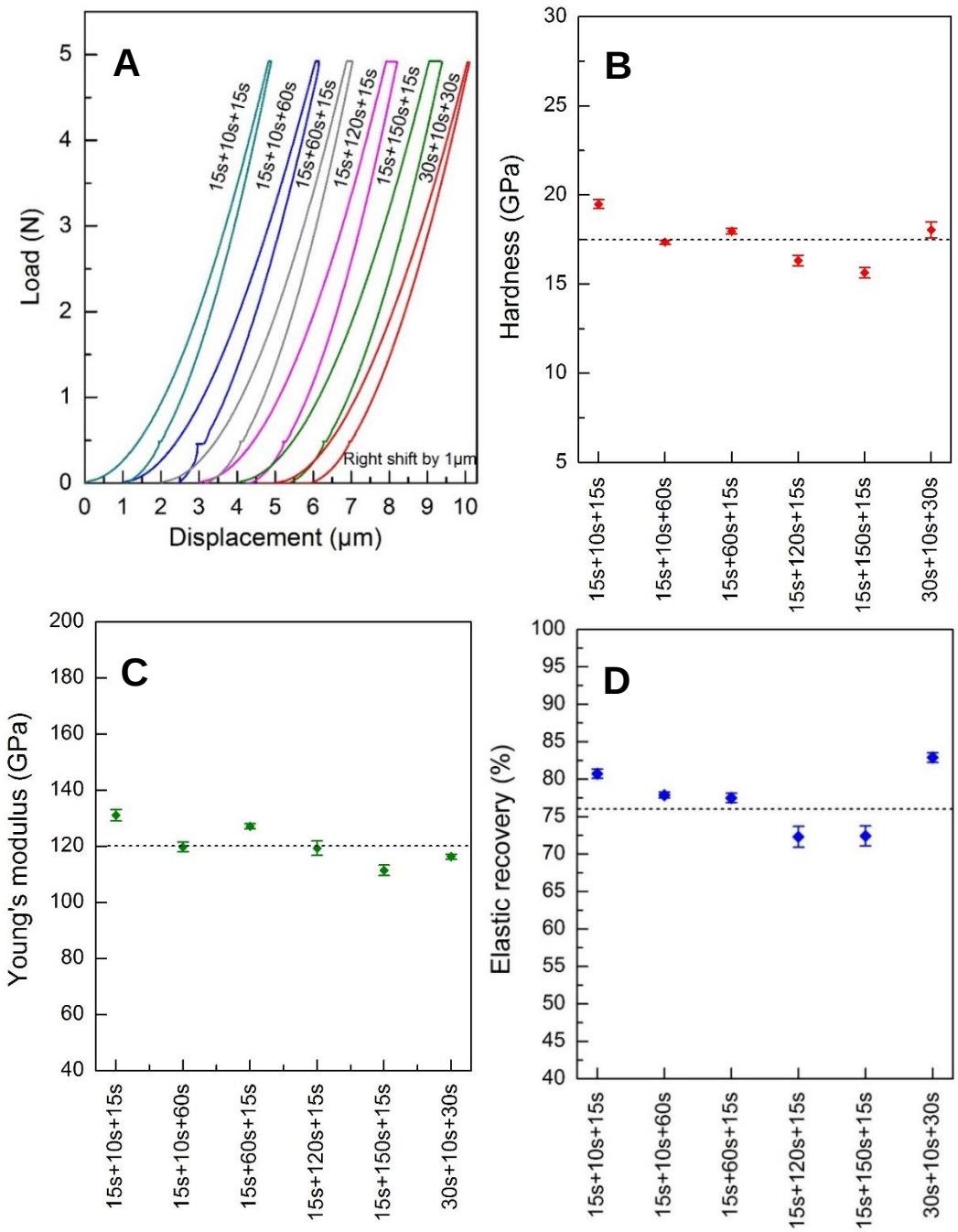

fig. S9. The loading/unloading-displacement curves, hardness, Young's modulus, and indentation elastic recovery of compressed GC at varied loading, holding, and unloading times. The results are shown in (**A**) to (**D**). The used compressed GC was produced at 25 GPa and 600 °C, having different batch with the *Com*.GC-2 indicated in text. The applied load was 4.9 N, and the three values shown, e.g. 15s+10s+15s, are loading, holding, and unloading times, respectively. The applied time has no significant effect on the mechanical properties, and the measurement accuracy is in a reasonable range.

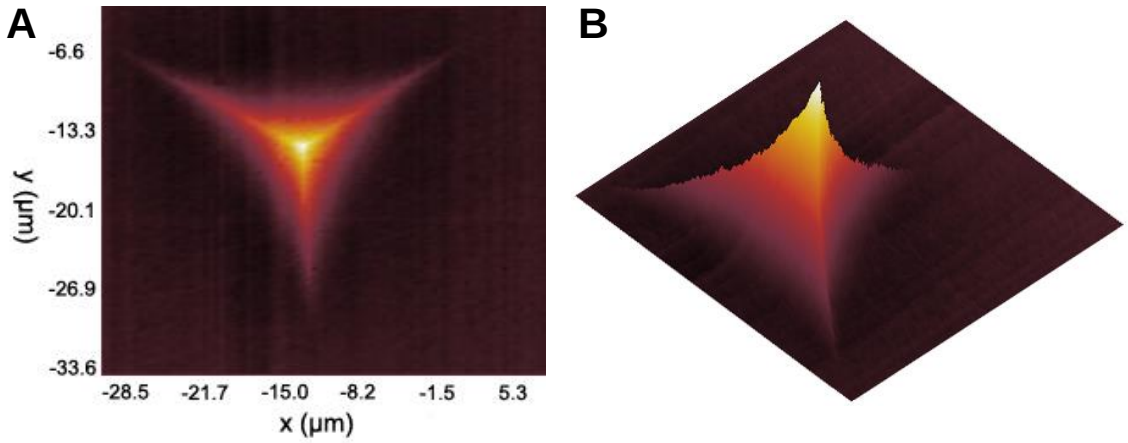

fig. S10. Indentation morphology after unloading three-sided pyramidal Berkovich diamond indenter, showing significant elastic recovery. (**A, B**) The 2D and 3D profiles of the impression. The sides of the indentation elastically recovered while the additional plasticity caused by the stress concentration at the edges of the indenter serves to permanently mark the position of the corners of the indentation at peak load.

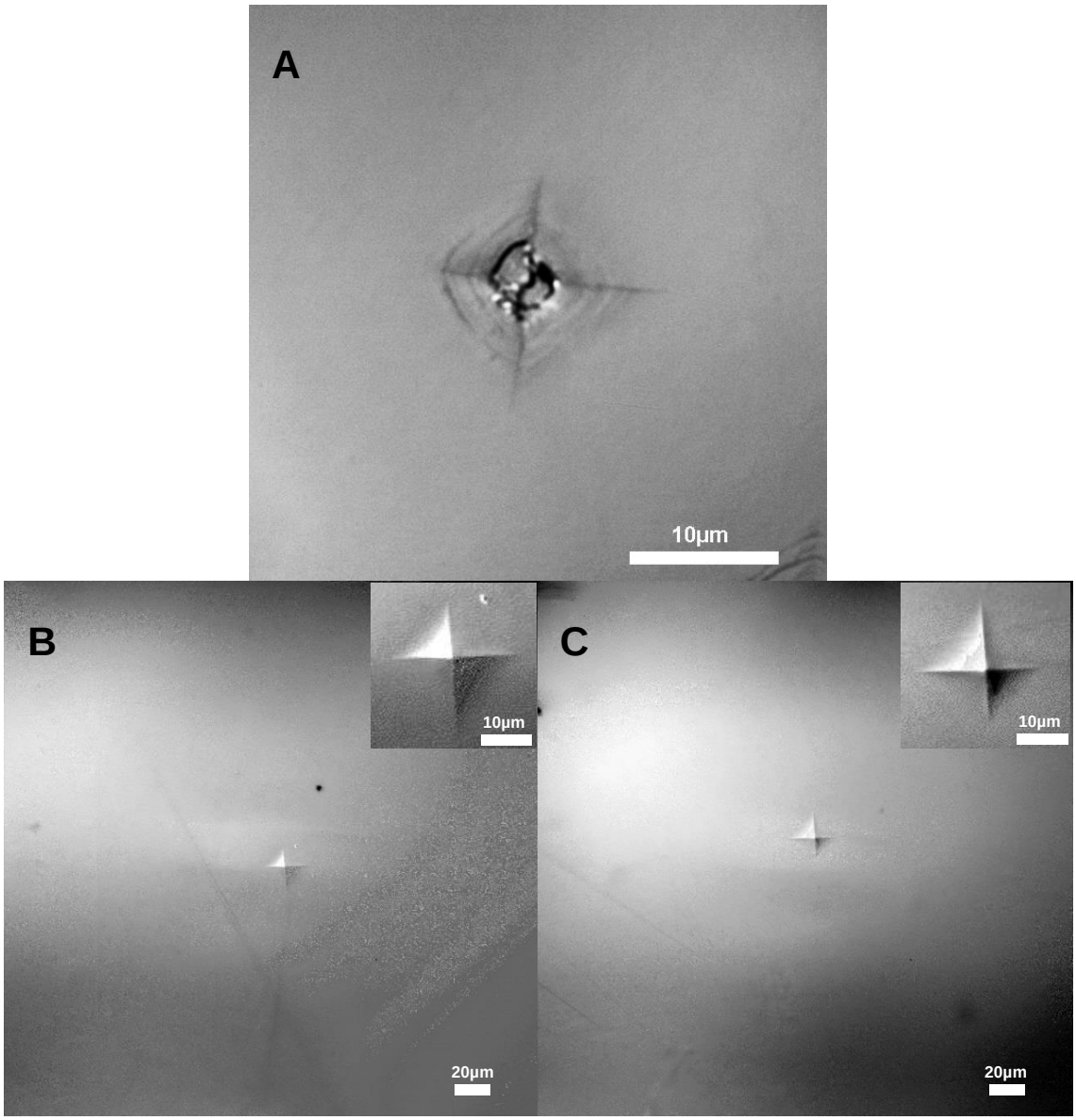

fig. S11. Optical images of the indentations on diamond and *Com*.GC-2 after unloading a four-sided pyramidal diamond indenter. The applied load was 4.9N. The loading and dwell times were both 15s. (**A**) The indentation left on the {111} face of a diamond single crystal shows obvious cracks. The measured Vickers hardness was 60 GPa, which is the usual value for diamond {111} face. (**B**, **C**) Two indentations left on randomly selected positions of *Com*.GC-2. The measured Vickers hardness of *Com*.GC-2 was 15.4 (±1.3) GPa, consistent with the result of indentation hardness obtained from the Berkovich diamond indenter. The insets show the enlarged indentation with no crack.

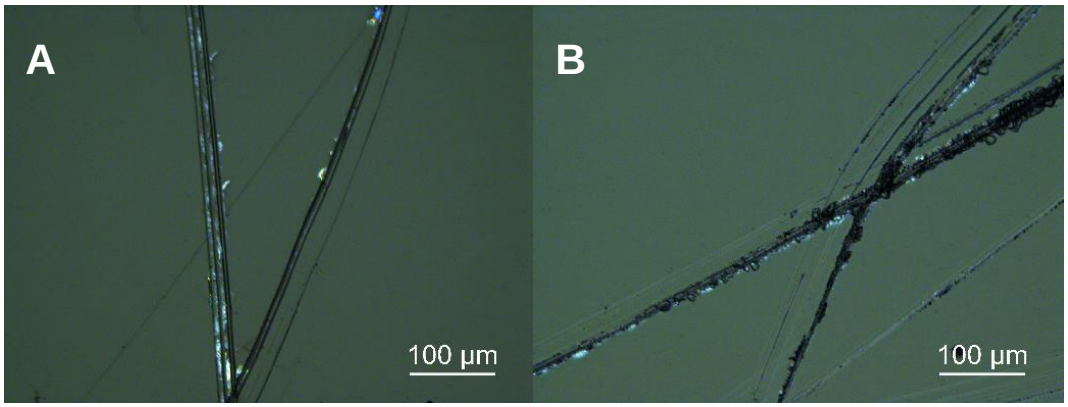

fig. S12. Mohs hardness of compressed GC (*Com*.GC-3) characterized with qualitative scratch tests. (**A**, **B**) Scratches left in the (0001) crystal planes of Al_2O_3 (Mohs scale: 9) and SiC single crystals (Mohs scale: 9.5), respectively. This means that the hardness of *Com*.GC-3 is comparable to or even higher than those of Al_2O_3 and SiC. The Vickers hardness of (0001) crystal planes of Al_2O_3 and SiC single crystals we measured are 22GPa, and 33GPa, respectively, which are consistent with other reports.

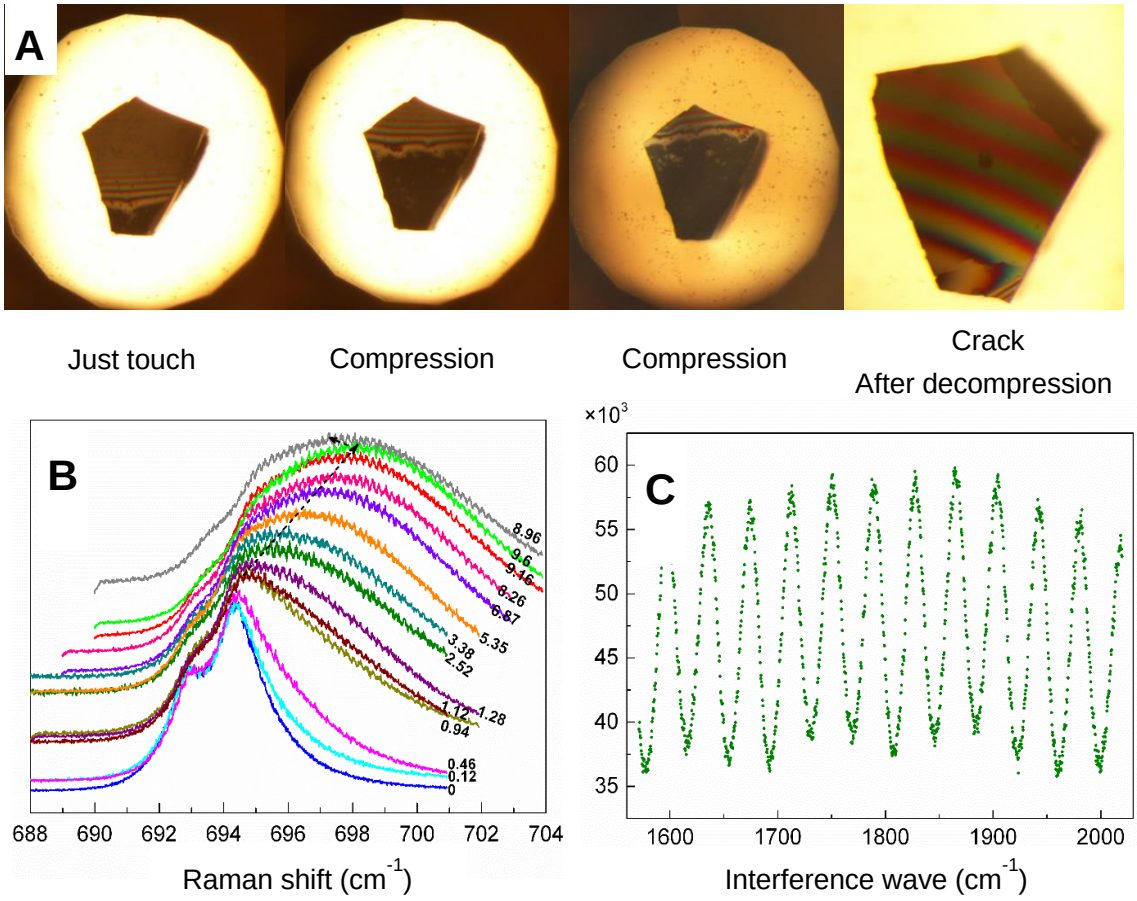

fig. S13. Axial compressive stress-strain relations established in a simple DAC. (**A**) Interference fringe change at sample surface during compression. When the diamond anvils touch the sample surface, the interference fringes disappear and the fine ruby becomes stressed. (**B**) Ruby fluorescence shifts from the surface of compressed GCs during compression. The arrow points to the change of center position of the R1 fluorescence peak indicating the pressure values according to the calibrated shifts with pressure (*26*). (**C**) Interference fringes originating from the light travel between the two diamond anvil surfaces. The spacing of adjacent fringes corresponds to two-times the distance between the diamond anvils, i.e., twice thickness of the sample.

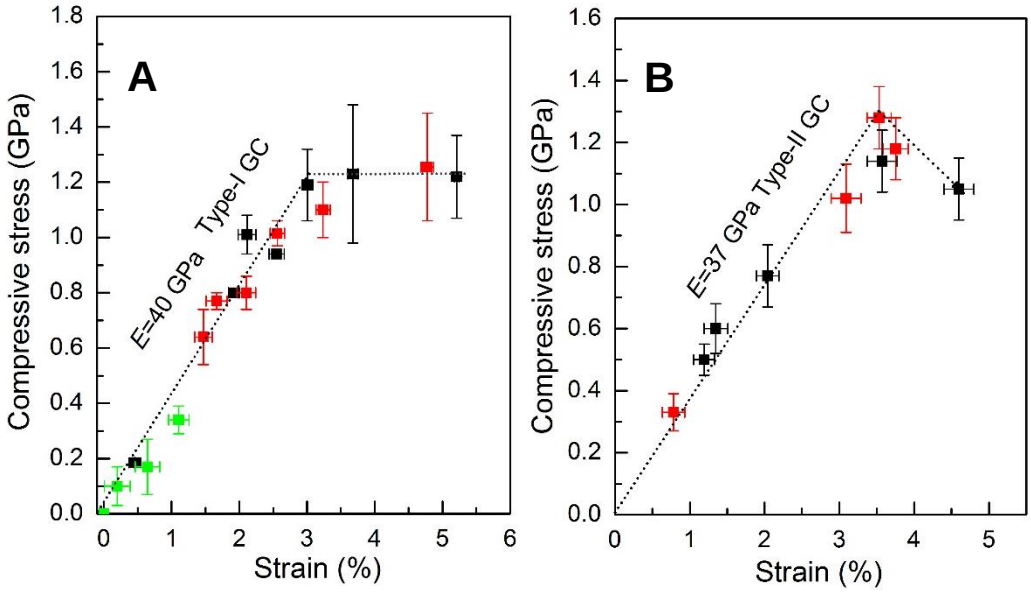

fig. S14. Compressive strength tests for standard materials including type I and II GCs in a simple DAC. (**A**, **B**) Compressive stress-strain curves of type-I and II GCs, respectively. The derived compressive strength and Young's modulus (*E*) are consistent with the published data (*10*), demonstrating the accuracy of the method.

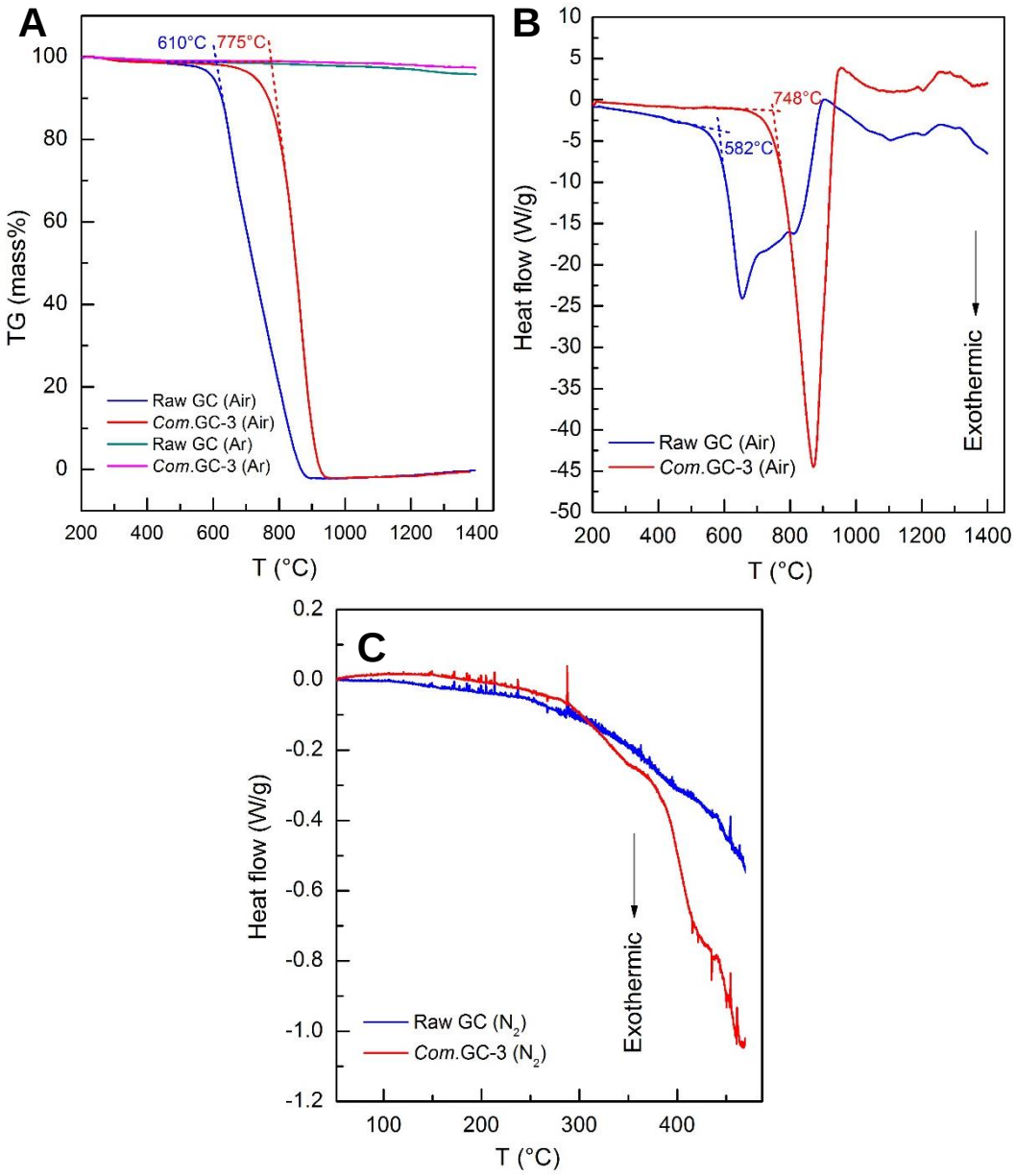

fig. S15. Comparison of thermal stability of compressed GC (*Com*.GC-3) with raw GC at air and inert argon (Ar) or nitrogen (N_2) conditions, respectively. (**A**) Thermogravimetry (TG) curves. The in-air oxidation temperatures were 775 °C for *Com*.GC-3 and 610 °C for raw GC. (**B**) The heat flow curves of DSC. The in-air oxidation temperatures were 748 °C for *Com*.GC-3 and 582 °C for raw GC. The above-measured oxidation temperatures are consistent with those determined from the thermogravimetry curves. The *Com*.GC-3 has a higher thermal stability than the raw GC at air condition, whose oxidation resistance temperature is about 160 °C higher than that of raw GC. At Ar condition, almost no mass change is found for both raw and compressed GCs up to the measurement temperature of 1400 °C, indicating their high stabilities at inert atmosphere. (**C**) The heat flow curves of DSC measured at inert condition. Both raw GC and compressed GC (*Com*.GC-3) release heat very slightly and similarly for temperature up to

300 °C, and the compressed GC releases more heat than raw GC does when temperature is higher than 300 °C. The extra and small heat release from *Com*.GC-3 sample may come from the relaxation of stress/strain.